Evaluation of Active and Passive UAV-Based Surveying Systems for Eulittoral Zone Mapping

Reuma Arav[a,b,*], Camillo Ressl[a], Robert Weiss[c], Thomas Artz[c], Gottfried Mandlburger[a]

[a] Dept. of Geodesy and Geoinformation, TU Wien, Vienna, Austria
[b] Institute of Geomatics, University of Natural Resources and Life Sciences, Vienna, Austria
[c] Federal Institute of Hydrology (BfG), Koblenz, Germany

Commission II, WG II/2

KEY WORDS: Topobathmetric LiDAR, Topographic LiDAR, photogrammetry, water exchange zone

ABSTRACT:

The eulittoral zone, which alternates between being exposed and submerged, presents a challenge for high-resolution characterization. Normally, its mapping is divided between low and high water levels, where each calls for a different type of surveying instrument. This leads to inconsistent mapping products, both in accuracy and resolution. Recently, uncrewed airborne vehicle (UAV) based photogrammetry was suggested as an available and low-cost solution. However, relying on a passive sensor, this approach requires adequate environmental conditions, while its ability to map inundated regions is limited. Alternatively, UAV-based topo-bathymetric laser scanners enable the acquisition of both submerged and exposed regions independent of lighting conditions while maintaining the acquisition flexibility. In this paper, we evaluate the applicability of such systems in the eulittoral zone. To do so, both topographic and topo-bathymetric LiDAR sensors were loaded on UAVs to map a coastal region along the river Rhein. The resulting point clouds were compared to UAV-based photogrammetric ones. Aspects such as point spacing, absolute accuracy, and vertical offsets were analysed. To provide operative recommendations, each LiDAR scan was acquired at different flying altitudes, while the photogrammetric point clouds were georeferenced based on different exterior information configurations. To assess the riverbed modelling, we compared the surface model acquired by the topo-bathymetric LiDAR sensor to multibeam echosounder measurements. Our analysis shows that the accuracies of the LiDAR point clouds are hardly affected by flying altitude. The derived riverbed elevation, on the other hand, shows a bias which is linearly related to water depth.

1. INTRODUCTION

Mapping the littoral zone is fundamental for coastline management, biodiversity conservation, climate change impact assessment, etc. (Taddia et al., 2020; Burdziakowski et al., 2020). This region, which is defined as the transition area between land and water environments, is generally characterised by three distinctive areas: sublittoral, which is constantly covered with water; supralittoral, which is never submerged; and the eulittoral, which interchanges between inundated and not inundated, depending on discharge levels or tidal events. Of these, the last is the most challenging for mapping. Different instruments are used to accommodate the ever-changing environment. Bathymetric instruments (e.g., multibeam echosounder) are used at high water levels, while topographic ones (e.g., topographic airborne laser scanners) are utilized at low water level (Li et al., 2023; Wang et al., 2023b). This leads to inconsistent mapping products, both in resolution and accuracy. To overcome this, airborne topo-bathymetric laser scanners (ALB) are increasingly deployed (Tysiac, 2020; Maas et al., 2019). Such an approach provides simultaneous mapping of the river/seabed, water surface, and dry land area, while maintaining homogeneous point density. Furthermore, the areal coverage depends only on flying altitude and is independent of water depth (Mandlburger et al., 2020). However, this solution is expensive and has preconditions, e.g., availability of a suitable aircraft and adequate environmental conditions.

In recent years, uncrewed aerial vehicles (UAVs) have been increasingly used for cost-effective acquisition of topographic datasets in general, and of the littoral regions in particular. These allow fast and inexpensive acquisition, as they overcome the limitations that exist for crewed airborne campaigns. Most works that use UAVs, utilize photogrammetric-based solutions for the task. For example, Taddia et al. (2020) and Bertin et al. (2022) used a UAV-borne camera to image and map a coastal section. The authors used structure-from-motion multi-view stereo (SfM-MVS) image matching techniques to generate photogrammetric point clouds. To improve the mapping accuracy, both studies post-processed GNSS observations taken during the flight, reaching a centimetre level accuracy. Specifically for the intertidal zone, Li et al. (2023) added evenly distributed ground control points along the study site to improve the georeferencing of the digital elevation model (DEM). However, image-based approaches are sensitive to lighting conditions and fall short in mapping submerged regions. In this regard, Wang et al. (2023a) tested the applicability of UAV-borne laser scanners for intertidal estuaries mapping. In this experiment, the authors extracted a centimetre-level DEM at a vertical accuracy of 5.5 cm.

In this paper we analyse the properties of data acquired by active and passive sensors loaded on a UAV at varying flying altitudes for eulittoral zone mapping. Furthermore, we compare between water penetrating laser scanners and non-penetrating ones. To do so, we use a topographic near-infrared (NIR) laser scanner and a green topo-bathymetric one. As a comparison, we evaluate an image-based generated point cloud, based on images captured by a DSLR camera at a 100 m above ground level (agl.). We estimate the effect of additional information used (e.g., control points, trajectory and INS information) on

* Corresponding author

the generated point clouds and consequently the DEM. Additionally, evaluation is carried out for the topo-bathymetric laser scanner in the sublittoral regions. There, we compare the acquired elevations to multibeam echosounder (MBES) measurements taken under the same conditions.

2. STUDY SITE AND MEASUREMENT CAMPAIGN

The site chosen for this study is an inland island within the river Rhein at Koblenz (Niederwerth). The study site itself is at the southern end of the island ($50°22'58''$ N, $7°36'55''$E, Figure 1). This site is characterised by an alluvial forest at its centre, no vegetation along the shorelines, and bushes in between. The shore itself is covered either by fine gravel or sand, and is approximately planar. The scans were carried out on Nov., 17, 2021.

Two UAVs were used for data acquisition. The first was loaded with a RIEGL VUX-1UAV NIR topographic laser scanner and a Sony Alpha 7rII camera (cf. Table 1 and Table 2), with a nominal ground sampling distance (GSD) of 1.8 cm at a flying altitude of 100 m agl. The second system was loaded with a topo-bathymetric RIEGL VQ-840-G (Table 1). Both UAVs were flown at three different heights: 50 m, 75 m, and 100 m agl. For simplicity, we will refer hereafter to the RIEGL VUX-1UAV scanner as Type-A whereas RIEGL VQ-840-G will be referred to as Type-B.

Three types of targets were used as ground control points (Figure 2), all measured with an RTK-GNSS: *i*) a cross point, whose centre was measured and marked by a pin; *ii*) a levelled planar 30 cm checkerboard, whose centre was measured, and *iii*) a roof-shaped target, where the two endpoints on the intersection line were measured. The dimensions of the two planes of the roof-target, as well as the angle between the planes, were measured in a lab. Note that both the checkerboard and roof-shape targets were positioned on a tripod, while the cross target was marked on the ground. The targets were distributed in eight places throughout the study site (Figure 1).

In addition, MBES were carried out by the (German) Federal Waterway and Shipping Administration in Dec., 2022. Of these, a 0.5 m grid of the riverbed was computed.

3. PRE-PROCESSING

3.1 Photogrammetric point clouds

Images captured at 100 m agl. were used to generate a point cloud and a DEM. To evaluate the effects of external information on the georeferencing of the generated point cloud, three processing configurations were used: using all control points without trajectory and INS information, using two cross control points with trajectory but without INS information, and lastly, using all cross control points, with trajectory and INS information (Table 3).

For these three variants, we used Metashape Agisoft to compute the bundle block adjustment and to generate the point clouds through dense image matching. The resulting point clouds were then classified to (dry) land; low, middle, and high vegetation; water; and unclassified. The classification was carried out based on the Type-A laser scanned point cloud acquired at 100 m agl.

3.2 LiDAR point clouds

Strip adjustment, classification, refraction correction, etc. were carried out using Airborne HydroMapping (AHM) software HydroVISH (Steinbacher et al., 2021).

Strip adjustment was carried out for each flying altitude and scanner type separately. To do so, points above the ground (e.g., outliers, vegetation, control points) were filtered out based on the hierarchical robust interpolation (Pfeifer and Mandlburger, 2018). Then an Iterative Closest Point to Plane (ICP) algorithm (Low, 2004) was computed. This way, a minimal distance and normal difference was achieved for points in the different strips.

Georeferencing was conducted based on all control points. However, due to lack of scanned points using Type-B at 50 m agl., this scan was not georeferenced and was excluded from further analysis.

Classification was focusing on classifying terrain and water-surface seed points. This was carried out by integrating several parameters, e.g., high point density, small point spacing, and distribution of false echoes. Other point attributes, such as the return number combined with the number of returns, were also used for seed points classification. For example, single-return points are classified as dry terrain seed points. To classify the riverbed seed points in Type-B point clouds, point attributes such as intensity (amplitude and reflectance) were used. These seed points served as the basis for further classification using morphological and surface-based filters (e.g., Pfeifer and Mandlburger, 2018; Lohmann et al., 2000).

Refraction For point clouds acquired with Type-B, a refraction correction was carried out for riverbed points. Setting the water and air refractive indices to $n_{water} = 1.33$ and $n_{air} = 1.000292$, as well as the water and air group velocities to $c_{air} = 299,710$ km/s and $c_{water} = 22,500$ km/s, we follow Mandlburger et al. (2013) for the refraction correction.

4. METHODS

To evaluate the quality of the different point clouds we examined the point distance, their absolute accuracy (with respect to the GNSS measured control points), and their vertical distance from a reference scan (see below). All assessments were carried out using the OPALS software (Pfeifer et al., 2014).

Point distance was estimated based on the number of points per square metre. However, as point density is uninformative at high numbers, we estimate the mean distance between two points. The relation between the number of points per square metre (D) and the mean distance a is $a = 1/\sqrt{D}$.

Absolute accuracy was estimated first by fitting a plane to points in the point cloud that are within 0.2 m radius from the GNSS-measured target. Then, the absolute accuracy was estimated as the perpendicular distance between the control point and the plane along the planes' normal direction. Note that for the roof targets, no RTK-GNSS points were measured directly on the target planes. Instead, only the two endpoints of the intersecting line were measured. Therefore, we developed a transformation workflow which allows the definition of a point on each target plane (see Appendix). The transformed points were then used as control points for further analysis. The checkerboard targets were removed from the absolute accuracy analysis. This is because a search radius as small as 0.2 cm would pick erroneous point below the tripod.

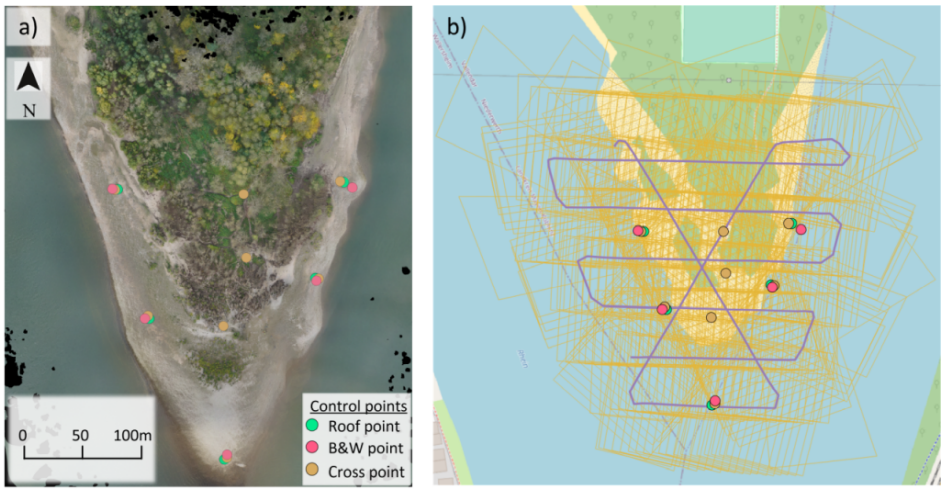

Figure 1. a) Orthophoto of the study site generated by the 100 m imaging flight. The different control points used are marked according to their type. b) Flight lines and images footprint overlaid upon OpenStreetMap base map.

	1UAV-VUX	VQ-840G
Flying speed [m/s]	5	5
Scanning angle (Field of view) [°]	90	40
Pulse repetition rate [kHz]	550	200
Accuracy [mm]	10	20
Precision [mm]	5	15
Wavelength	1550 nm, NIR	532 nm, green
IMU System	APPLANIX AP20	APPLANIX APX20
System Weight [kg]	5.5	12

Table 1. Scanning and flying specifications for the two scanning systems used. Each system was flown at altitudes of 50 m, 75 m, and 100 m.

Sony Alpha 7rII	
Pixel dimensions	7952× 5304
Sensor Type [mm]	CMOS 25.9× 24.0
Sensor Size [mm]	35.9 × 24.0
Lens	ZEISS Batis 2/25
Focal length	25mm
GSD	1.8 cm at 100 m flying height
System Weight [kg]	1.2

Table 2. Properties of the camera used for the photogrammetric campaign.

Variant	Description
HighEnd	100 m Flight altitude agl., all CPs, with GNSS-trajectory (including INS)
Standard	100 m Flight altitude agl., 2 cross points, with GNSS-trajectory (without INS)
LowEnd	100 m Flight altitude agl., all cross points, without trajectory

Table 3. Description of the three georeferencing configurations of the photogrammetric point clouds.

DEM assessment. To assess the similarity between the scans, DEMs were generated at 0.04 m grid size, with 16 closest neighbours. Vegetation was filtered out from all point clouds using the hierarchic robust interpolation (Pfeifer and Mandlburger, 2018). Type-A at 50 m agl. was chosen as the reference for comparison. The DEM assessment was carried out by computing the DEM of Differences (DoD) of the various DEMs and the reference one.

Comparison to MBES. To compare between MBES and the topo-bathymetric LiDAR measurements of the riverbed, a DEM of the riverbed was created from the MBES measurements (0.5 m grid size). A corresponding 0.5 m grid size DEM of the riverbed was generated from the points acquired in the water area from Type-B scanner at 100 m agl. after refraction correction. Then, we computed the DoD between the two models and estimated the water depth based on the MBES DEM.

5. RESULTS AND DISCUSSION

5.1 Point distance

When comparing Type-A and Type-B datasets, Type-A should have higher spatial resolution. This is mostly due to its higher ground point coverage and smaller laser footprint (Mandlburger, 2020; Mandlburger et al., 2022). However, this sensor has a longer pulse duration and thus a larger minimum distance between two consecutive echoes or laser points (range discrimination distance). Therefore, Type-B might have a higher number of echoes in vegetated areas. To investigate this, we estimated the point distance.

Figure 3 shows the average point spacing of point clouds generated by the various sensors at flight altitude of 100 m agl. Ana-

Figure 2. Examples of the different control points: a) cross ; b) checkerboard; and c) roof. d) The three target types used for the analysis as captured from the air.

lysis showed that point distances at the different tested configurations (both LiDAR and photogrammetric) follow the same pattern. Therefore, only one representative of each sensor is shown here. For the sake of consistency, we present the results for a flying altitude of 100 m for all sensors. For the photogrammetric point cloud, the HighEnd configuration is shown. The estimation was carried out based on a 0.25 m and 0.1 m grid for the photogrammetric and LiDAR point clouds, respectively. It can be seen that the mean point distance in the photogrammetric point cloud is much lower, reaching 1 cm in most places. As for the LiDAR acquired point clouds, the distance is mostly lower than 0.5 cm. Note, however, that the nearly elliptic scan pattern of Type-B dictates the point distance.

Figure 4 shows a histogram of the mean distance for the various point clouds at 100 m agl. It can be seen that the points acquired by Type-A sensor have the most uniform spatial spacing between them. Ninety percent of the points are up to 2 cm apart, with a mean spacing of 1.9 ± 0.4 cm and a median of 1.8 cm. The photogrammetric point cloud is the least uniform.

5.2 Absolute accuracy

Photogrammetric point clouds. We begin with a comparison of the absolute accuracy of the photogrammetric point clouds generated using different georeferencing configurations.

Table 4 shows the vertical offset of the cross points from the nominal height. As these targets are located on an approximately horizontal terrain, the comparison shows the absolute height accuracy. The largest offsets are 4.5 cm and 4.4 cm for target no. 108 and 106, respectively, both in the point cloud generated with Standard configuration. It should be noted that both targets yielded the largest offsets in other configurations as well. The average offset for the Standard configuration is considerably higher than the others. The LowEnd configuration yielded the highest accuracy. This is probably due to the fact that only crosses were used for the geo-referencing, and thus the point cloud is optimized to ground level. However, in all of the configurations, the magnitude of the offsets (i.e., mean absolute error) is similar, of 1.5 ± 5 cm.

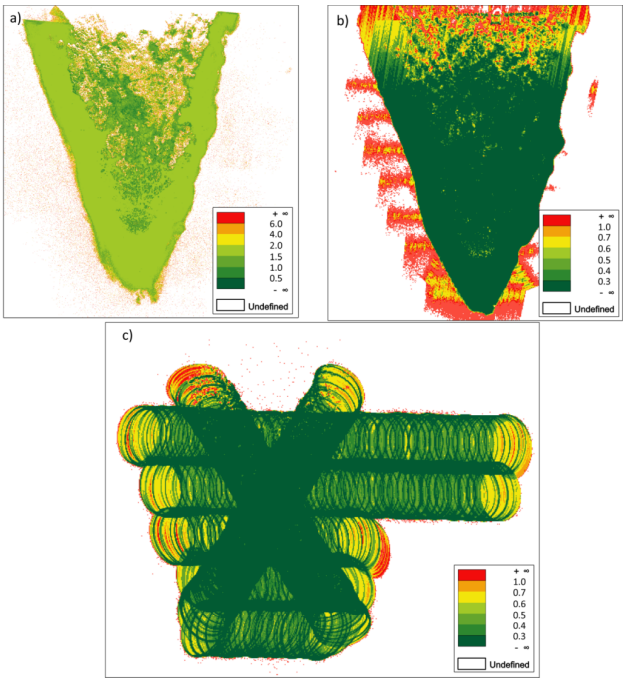

Figure 3. Mean point distance [cm] at 100 m altitude: a) Photogrammetric ; b) Type-A; c) Type-B. Note the different colour scales between the LiDAR/photogrammetric point clouds: in the photogrammetric one, the point distance in open areas corresponds to the 1.8c m GSD (between 1.5-2.0 cm).

Table 5 shows the 3D offsets of the different point clouds from the roof targets. Unlike the cross targets, here the planes on which the points lie are not aligned with the Z-axis. Consequently, the offset values includes both vertical and planimetric accuracies. For that reason, the values are higher than those of the cross targets. The largest offset values are -5.7 cm and -5.3 cm, both for target 316, for the LowEnd and Standard configurations, respectively. Generally, the LowEnd configuration yielded the lowest absolute accuracy. This can be attributed to the fact that no parameters which affect the height determination are used for the geo-referencing (i.e., neither the roof targets nor the trajectory). The point clouds generated using the Standard configuration yielded the lowest mean offset (i.e., systematic bias) of -1.6 cm. Looking at the magnitude of the offsets, it is estimated at approximately 2.0 cm for all configurations.

ID	HighEnd	Standard	LowEnd
101	2.1	2.6	0.3
102	0.6	1.9	-0.6
103	-0.8	-0.9	-0.9
104	-0.5	0.2	-0.5
105	-0.3	0.6	0.1
106	2.8	4.4	2.0
107	-3.1	-0.7	-1.7
108	1.9	4.5	2.0
Mean	0.3	1.5	0.1
Std.†	1.9	1.6	1.3
MAE. ‡	1.5	2.0	1.0

Table 4. Offset values [cm] between cross targets and the fitted plane in the point cloud for the different photogrammetric point clouds. † Standard deviation; ‡ Mean absolute error.

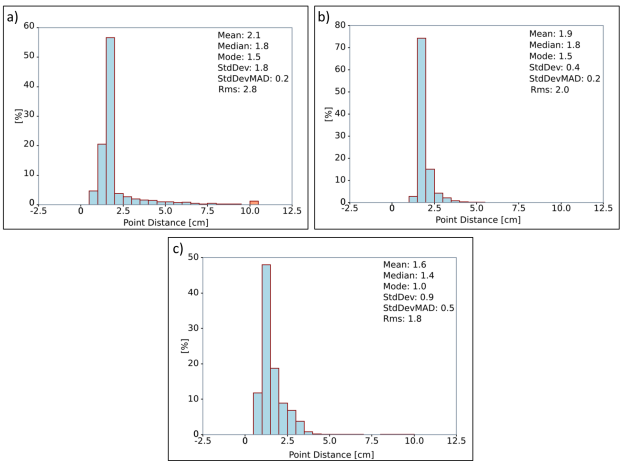

Figure 4. Average point distance distribution at 100 m flying altitude: a) Photogrammetric point cloud; b) Type-A; c) Type-B.

ID	HighEnd	Standard	LowEnd
300	-1.8	-0.5	-1.7
306	0.4	-1.0	-2.3
310	-2.2	1.1	-2.3
314	-2.8	-2.6	-2.3
316	-3.1	-5.3	-5.7
322	1.7	0.8	0.1
326	-4.5	-3.6	-3.7
330	-2.8	-1.5	-1.7
334	-2.5	-2.3	-3.6
338	-0.6	-0.8	0.8
Mean	-1.8	-1.6	-2.2
Std.†	1.8	2.0	1.9
MAE. ‡	2.2	2.0	2.4

Table 5. Offset values [cm] between roof targets to the closest point in the point cloud in the different photogrammetric point clouds.
† Standard deviation; ‡ Mean absolute error.

Generally, it can be said that the absolute accuracy of the photogrammetric point cloud does not exceed 2 cm, which corresponds to approx. 1 pixel. Moreover, the HighEnd configuration did not show any improvement in the results.

LiDAR point clouds. Table 6 presents the vertical offset values for all scanning flight configurations. For Type-A, the same average values are received, in the range of 0.1 cm. Nonetheless, the magnitude of the offsets stands on 1.0 cm for all Type-A scans. As for Type-B, there the average offset is at the range of -1.0 cm. The largest deviation stands on -3.3 cm, also for target 107, at altitude of 100 m agl. The offset magnitude here is about 1.7 times larger than that of Type-A at corresponding altitudes.

The values in Table 7 confirm that Type-A sensor achieves a centimetre accuracy, with mean values close to zero (0.0-0.4), it shows that there are no systematic deviations. The average of the absolute values is 1.0 cm for all point clouds. This means that the increase in altitude does not lead to a decrease in absolute accuracy. For Type-B sensor, the maximum deviations are 6.9 cm and 6.3 cm from flight altitudes of 75 m and 100 m agl., respectively. Although there is no clear difference in the maximum offsets between the two flight altitudes, the mean values show an increase proportional to the flight altitude (29 mm @ 75 m, 39 mm @ 100 m). On average, the values are still

	Typ-A			Typ-B	
Target no.	50 m	75 m	100 m	75 m	100 m
101	-0.6	0.8	-0.1	-2.6	-0.8
102	0.7	0.7	0.1	1.5	2.2
103	0.5	-0.2	-1.1	-1.2	-2.3
104	1.2	0.5	1.0	1.0	-2.2
105	-0.8	-1.5	-0.9	-2.6	-1.2
106	1.6	1.6	1.1	0.9	-0.2
107	-2.2	-2.0	-2.0	-2.7	-3.3
108	0.6	0.7	0.5	-1.4	-0.2
Mean	0.1	0.1	-0.2	-0.9	-1.0
Std.†	1.2	1.2	1.0	1.7	1.6
MAE.‡	1.0	1.0	0.9	1.7	1.5

Table 6. Vertical offset values [cm] between cross targets to the closest point in the point cloud of the individual flight scans.
† Standard deviation; ‡ Mean absolute error.

	Typ-A			Typ-B	
Target no.	50 m	75 m	100 m	75 m	100 m
300	-3.5	-	-2.4	0.2	4.9
306	0.7	0.2	0.2	4.0	1.3
310	0.5	-0.6	-0.3	2.7	5.6
314	-0.8	0.9	-	-1.2	2.9
316	1.9	1.1	2.0	5.0	6.1
322	1.8	1.8	2.1	-0.8	1.5
326	-0.2	-0.3	0.5	3.1	3.2
330	0.6	0.5	1.2	5.6	2.3
334	-0.2	0.5	0.1	0.9	6.3
338	-0.3	-1.4	-0.1	6.9	4.9
Mean	0.0	0.3	0.4	2.9	3.9
Std.†	0.9	1.0	0.9	3.0	1.6
MAE.‡	1.0	0.7	0.9	3.0	2.9

Table 7. Offset values [cm] between the LiDAR point clouds and the roof control points (measured along the normal) for each flight configuration.
† Standard deviation; ‡ Mean absolute error.

well below 5 cm. It should be noted that the roof-planes were too small for this sensor. This must be also taken into account when interpreting the above results.

For both types, no significant differences can be observed for the individual altitudes. Therefore, from the point of view of measurement accuracy, the more efficient flight altitude of 100 m has no disadvantages.

Since the offset is being computed by fitting a plane to a neighbourhood in the vicinity of the control points, we also compared the root mean square error (RMSE) of the fitted plane. This measure can be seen as signifying the amount of noise in the point cloud (i.e., precision). It can be seen that the photogrammetric point clouds show higher precision than the LiDAR-based ones (Figure 5). The highest RMSE is in the range of 1 cm for Type-B. The photogrammetric point clouds, on the other hand, show the lowest RMSE, only of a few millimetres. This is probably due to the fact their generation uses a semi-global matching, which performs averaging in the end.

5.3 DEM assessment

The DoDs of the different photogrammetric configuration exhibited similar results. Therefore, Figure 6 shows only the DoD of the Standard configuration. It can be seen that the largest differences are at the vegetated areas, even though the vegetation

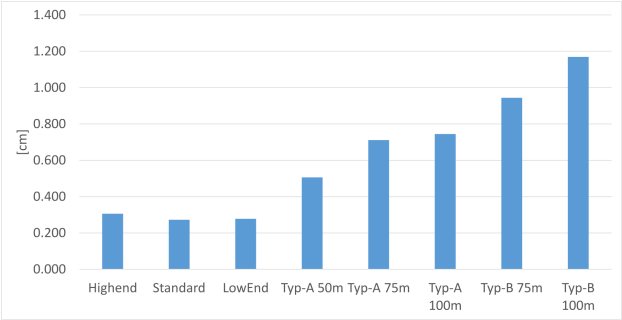

Figure 5. RMSE [cm] of the fitted plane around the cross control points.

was removed. The north-western part is higher by up to 6 cm than the reference DEM. These discrepancies are probably due to the fact that the control points were distributed mainly in the southern region of the study area. For all photogrammetric-base DEMs, most of the terrain shows a discrepancy of up to 5 cm. This can be due to the fact that in this gravel dominant regions, the photogrammetric point clouds reconstruct the top part of the gravel, whereas the LiDAR point cloud also records points in-between. Such an effect was documented and discussed in Ressl et al. (2016).

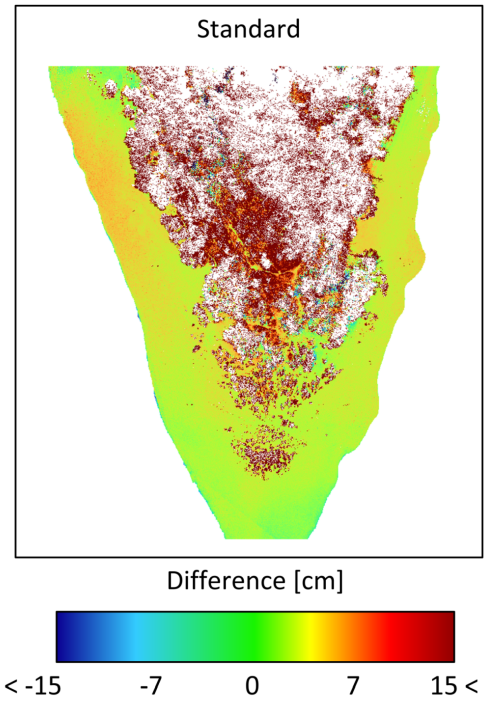

Figure 6. DoD between standard configuration photogrammetric-based DEMs and Type-A at 50 m altitude DEM.

Figure 7 presents the DoDs of the LiDAR-based variants and the reference DEM. Here too, the vegetated area exhibits higher discrepancies. Type-B at 75 m altitude shows difference of approx. 15 cm from the reference DEM along the western shoreline, directly at the water-land line.

Statistical analysis of the different DoDs shows that the mean differences between the DEMs and the reference DEM are higher for those based on the photogrammetric point cloud (Table 8). These reach up to a 1.8 cm (for the HighEnd con-

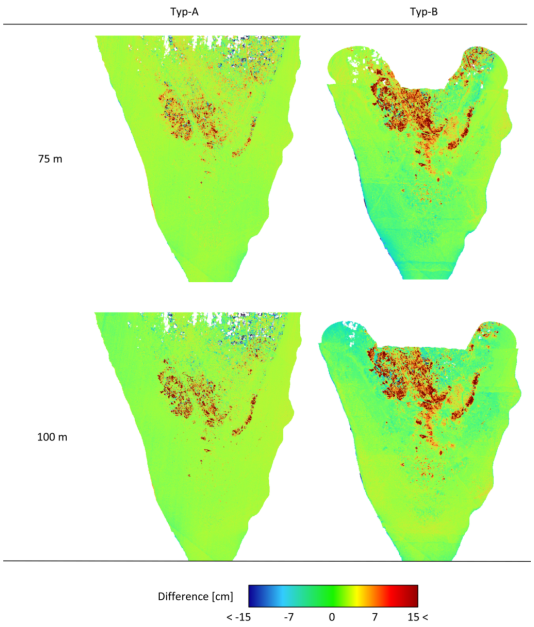

Figure 7. DoD between LiDAR-based DEMs and Type-A at 50 m altitude DEM.

		Mean [cm]	Std. [cm]
Photogrammetric	HighEnd	1.8	3.7
	Standard	1.2	3.7
	LowEnd	1.1	3.7
Type-A	75 m	-0.1	4.3
	100 m	0.2	4.0
Type-B	75 m	0.1	5.1
	100 m	0.1	5.2

Table 8. Mean and standard deviation of the discrepancies between the reference DEM and the various DEMs.

figuration), as opposed to a maximum of 0.2 cm for Type-A (at 100 m agl. altitude). The height difference standard deviation for the photogrammetric point clouds, regardless of the georeferencing configuration, is the same (3.7 cm), almost double the GSD. Similarly, the different flight altitudes hardly affect the standard deviation of the LiDAR-base DEMs, reaching approx. 4 cm and 5 cm for Type-A and Type-B based DEMs, respectively (Table 8).

5.4 Comparison to MBES

Figure 8 shows a scatter plot of the vertical difference between points at the water area scanned by Type-B at 100 m flight altitude and the MBES measurements of the same region as a function of the water depth. It can be seen that a linear relationship exists ($R^2 = 0.89$). A computation of a regression line (marked in red) yields an intercept of $d = 0.07$ and a slope value of $k = 0.046$. The small intercept means that there is no significant height deviation in shallow waters. This is an indication of both correct water surface classification and precise water surface modelling. The approx. 5% slope proves an overestimation of the water depth by the Type-B sensor, assuming that the MBES provides the correct water depth. Therefore, we can conclude that a larger refraction index of the water should be used for the refraction correction (i.e., > 1.4). From a physical point of view, this observation is not plausible. However, it is consistent with the findings of Mandlburger et al. (2020). One

possible reasoning for this systematic error can be the multiple forward scattering effects. However, further analysis is required to better understand this effect. Such an experiment is currently underway. It should be noted, that this systematic error has been observed only for UAV-borne LiDAR and not for manned systems in shallow water.

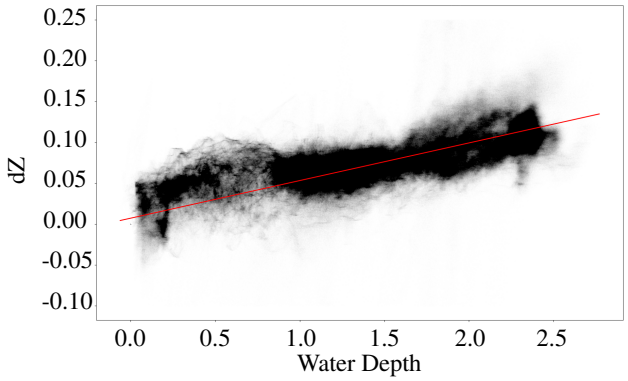

Figure 8. Scatterplot of the two computed attributes: water depth and vertical difference (dZ), overlaid with a regression line ($y = 0.046x + 0.007$, R^2=0.89).

6. CONCLUSIONS

In this paper we have shown an evaluation of passive and active UAV-based surveying systems to map littoral regions in general, and eulittoral ones in particular. The evaluation included mean point distance, absolute accuracy, as well as DEM validation. We have shown that the point distance in the photogrammetric point cloud corresponds to the nominal GSD of 1.8 cm. As for the LiDAR point clouds, the VUX-1UAV showed the most uniform point spacing of 1.9 cm. The VQ-840-G sensor provided a denser point cloud with a median point spacing of 1.4 cm.

Evaluating the required external information for georeferencing the photogrammetric point clouds, we tested three levels of exterior information. The results have shown that all three georeferencing configurations yielded similar absolute accuracy of approx. 2 ± 1.5 cm when compared to the check points. When compared to the reference DEM, the accuracy was of 1 ± 3.7 cm. Therefore we conclude that using the Standard configuration, which uses only two cross points but also incorporates the GNSS trajectory, would be the best approach.

The LiDAR-based point clouds were acquired at three different flying altitudes. Results have shown that these did not affect the absolute accuracy, reaching approx. 0.1 ± 1 cm and 1.5 ± 3 cm for the VUX-1UAV (Type-A) and the VQ-840-G (Type-B) sensor, respectively. Similar results were received when comparing the DEMs. Therefore, we can recommend a flying altitude of 100 m, which allows larger coverage at the same accuracy level.

Lastly, we compared the riverbed surface model acquired by the topo-bathymetric LiDAR to a multibeam echosounder measurements. Results have shown that there is a linear relation between water depth and height offset. The VQ-840-G sensor overestimates the water depth, making its usage problematic without a reference. A respective experiment under laboratory conditions is currently a work in progress. The experiment investigates if a relationship between signal propagation speed and turbidity can be established.

REFERENCES

Bertin, S., Stéphan, P., Ammann, J., 2022. Assessment of RTK Quadcopter and Structure-from-Motion Photogrammetry for Fine-Scale Monitoring of Coastal Topographic Complexity. *Remote Sensing*, 14(7), 1679.

Burdziakowski, P., Specht, C., Dabrowski, P. S., Specht, M., Lewicka, O., Makar, A., 2020. Using UAV Photogrammetry to Analyse Changes in the Coastal Zone Based on the Sopot Tombolo (Salient) Measurement Project. *Sensors*, 20(14), 4000.

Li, Y., Wu, Y., Sun, Z., Zhao, D., Yu, C., Li, Y., You, G., Kong, Z., Xi, X., Lei, L., 2023. Using UAV imagery to generate DEMs of the intertidal zone. *Journal of Coastal Conservation*, 27(3).

Lohmann, P., Koch, A., Schaeffer, M., 2000. Approaches to the filtering of laser scanner data. *International Archives of Photogrammetry and Remote Sensing*, 33(B3/1; PART 3), 540–547.

Low, K.-L., 2004. Linear least-squares optimization for point-to-plane icp surface registration. *Chapel Hill, University of North Carolina*, 4(10), 1–3.

Maas, H.-G., Mader, D., Richter, K., Westfeld, P., 2019. IMPROVEMENTS IN LIDAR BATHYMETRY DATA ANALYSIS. *The International Archives of the Photogrammetry, Remote Sensing and Spatial Information Sciences*, XLII-2/W10, 113–117.

Mandlburger, G., 2020. A review of airborne laser bathymetry for mapping of inland and coastal waters. *Hydrographische Nachrichten*, 116(06/2020), 6–15.

Mandlburger, G., Monetti, D., Greifeneder, C., 2022. Fließgewässervermessung mittels UAV-basierter Laserbathymetrie im Produktiveinsatz. *Österreichische Zeitschrift für Vermessung und Geoinformation (VGI)*, 2022(2), 59–77.

Mandlburger, G., Pfennigbauer, M., Pfeifer, N., 2013. Analyzing near water surface penetration in laser bathymetry – A case study at the River Pielach. *ISPRS Annals of the Photogrammetry, Remote Sensing and Spatial Information Sciences*, II-5/W2, 175–180.

Mandlburger, G., Pfennigbauer, M., Schwarz, R., Flöry, S., Nussbaumer, L., 2020. Concept and Performance Evaluation of a Novel UAV-Borne Topo-Bathymetric LiDAR Sensor. *Remote Sensing*, 12(6), 986.

Pfeifer, N., Mandlburger, G., 2018. *Topographic Laser Ranging and Scanning Principles and Processing, Second Edition*. Taylor & Francis Group.

Pfeifer, N., Mandlburger, G., Otepka, J., Karel, W., 2014. OPALS – A framework for Airborne Laser Scanning data analysis. *Computers, Environment and Urban Systems*, 45, 125–136.

Ressl, C., Brockmann, H., Mandlburger, G., Pfeifer, N., 2016. Dense Image Matching vs. Airborne Laser Scanning – Comparison of two methods for deriving terrain models. *Photogrammetrie - Fernerkundung - Geoinformation*, 2016(2), 57–73.

Steinbacher, F., Dobler, W., Benger, W., Baran, R., Niederwieser, M., Leimer, W., 2021. Integrated Full-Waveform Analysis and Classification Approaches for Topo-Bathymetric Data Processing and Visualization in Hydro-VISH. *PFG – Journal of Photogrammetry, Remote Sensing and Geoinformation Science*.

Taddia, Y., Stecchi, F., Pellegrinelli, A., 2020. Coastal Mapping Using DJI Phantom 4 RTK in Post-Processing Kinematic Mode. *Drones*, 4(2), 9.

Tysiac, P., 2020. Bringing Bathymetry LiDAR to Coastal Zone Assessment: A Case Study in the Southern Baltic. *Remote Sensing*, 12(22), 3740.

Wang, C., Morgan, G. R., Morris, J. T., 2023a. Drone Lidar Deep Learning for Fine-Scale Bare Earth Surface and 3D Marsh Mapping in Intertidal Estuaries. *Sustainability*, 15(22), 15823.

Wang, J., Wang, L., Feng, S., Peng, B., Huang, L., Fatholahi, S. N., Tang, L., Li, J., 2023b. An Overview of Shoreline Mapping by Using Airborne LiDAR. *Remote Sensing*, 15(1), 253.

APPENDIX

We assume a symmetric roof-shaped target, which is always stationed so that the intersection line is levelled. In the field, only the two endpoints along this line were measured by RTK-GNSS. To compute two point coordinates which lie on each of the roof planes we will use the two points $\mathbf{Q}_1$ and $\mathbf{Q}_2$ measured by RTK-GNSS at the endpoints of the intersection line. These define the object-space.

We define a model-space based on lab measurements. There, eight points were measured on each plane facet (the endpoints on the intersection line were measured twice). Using Principal Component Analysis (PCA) of the covariance matrix created from the four points on each plane we estimate the two normals $\mathbf{n}^{1,2}$:

$$\begin{aligned} \mathcal{C}^k &= \frac{1}{4}\sum_{i=1}^{4}(\boldsymbol{p}_i^k - \overline{\boldsymbol{p}}^{\boldsymbol{k}})\cdot(\boldsymbol{p}_i - \overline{\boldsymbol{p}}^k)^T, \\ \mathcal{C}^k \cdot \mathbf{v}_j^k &= \lambda_j \cdot \mathbf{v}_j^k,\ j \in \{0,1,2\} \end{aligned} \tag{1}$$

where $\mathbf{p}_i^k$ is point i on plane $k = 1, 2$ and $\overline{\mathbf{p}}^k$ represents the 3D centroid of the points on plane k. The normal $\mathbf{n}^k$ will then be the eigenvector $\mathbf{v}^k$ that belongs to the minimal eigenvalue. We then find the direction of the intersection line $\overline{\ell}_0$ in the model-space:

$$\overline{\ell}_0 = \mathbf{n}_1 \times \mathbf{n}_2. \tag{2}$$

Next, we define a point $\mathbf{q}_0$ on the line $\overline{\ell}_0$. Since the roof target in the lab is levelled, we can define the point $\mathbf{q}_0 = \begin{bmatrix}0 & 0 & 0\end{bmatrix}$ on $\overline{\ell}_0$.

We now define two more direction lines, $\overline{\ell}_1$ and $\overline{\ell}_2$, on each of the two target planes. These are orthogonal to $\mathbf{n}_1$ and $\mathbf{n}_2$, respectively, i.e.,

$$\overline{\ell}_1 = \overline{\ell}_0 \times \mathbf{n}_1 \tag{3}$$

$$\overline{\ell}_2 = \overline{\ell}_0 \times \mathbf{n}_2. \tag{4}$$

Any point on each plane will be a linear combination of the orthogonal lines, i.e.,

$$\mathbf{x}_{1,2} = \mathbf{q}_0 + a\overline{\ell}_0 + b\overline{\ell}_{1,2} \tag{5}$$

with a and b scalars and the subscripts refer to the first or second plane of the roof target in model-space. Note that as we are looking for arbitrary points on each plane, we use $\mathbf{q}_0$ at the origin.

Next, we define the 3D rigid-body transformation $\mathbf{X}_{1,2} = \mathbf{t} + \mathcal{R}\mathbf{x}_{1,2}$ from model- to object-space, where $\mathbf{t}$ is the translation and $\mathcal{R}$ the rotation matrix. To estimate the transformation parameters we first define the direction of the intersection line $\overline{\ell}_W$ in object-space using $\mathbf{Q}_1$ and $\mathbf{Q}_2$. Then, the intersection line in object-space is:

$$\overline{\ell}_W = \frac{\mathbf{Q}_2 - \mathbf{Q}_1}{||\mathbf{Q}_2 - \mathbf{Q}_1||} \tag{6}$$

The translation between the two systems is $\mathbf{t} = \mathbf{Q}_1$ (as $\mathbf{q}_0$ is at the origin). Assuming that the intersection line is levelled, the rotation between the two lines $\overline{\ell}_0$ to $\overline{\ell}_W$ is horizontal, i.e.,:

$$\mathcal{R} = \begin{pmatrix} \cos\theta & -\sin\theta & 0 \\ \sin\theta & \cos\theta & 0 \\ 0 & 0 & 1 \end{pmatrix} \tag{7}$$

which is equivalent to:

$$\mathcal{R} = \begin{pmatrix} \overline{\ell}_0 \cdot \overline{\ell}_W & -\|\overline{\ell}_0 \times \overline{\ell}_W\| & 0 \\ \|\overline{\ell}_0 \times \overline{\ell}_W\| & \overline{\ell}_0 \cdot \overline{\ell}_W & 0 \\ 0 & 0 & 1 \end{pmatrix}. \tag{8}$$

Because of the symmetric shape and since we use $||\overline{\ell}_W \times \overline{\ell}_0||$, there is a direction ambiguity. Therefore, to ensure that the points after transformation lie on the planes in object-space, we set $a = \pm\frac{1}{2}A$ and $b = \pm\frac{1}{2}B$ in Eq. (5), with A and B the width and length of each facet, as measured in the lab. This way, four points are defined on each plane, but only one is close to a point on the plane in the point cloud. This point is found by a simple neighbours search after the 3D rigid-body transformation.